3-2018

# Liquid-like thermal conduction in intercalated layered crystalline solids

B. Li
*Japan Atomic Energy Agency*

H. Wang
*University of California, Irvine*

Y. Kawakita
*Japan Atomic Energy Agency*

Q. Zhang
*Iowa State University and Ames Laboratory*

M. Feygenson
*Jülich Center for Neutron Science*

***See next page for additional authors***

# Liquid-like thermal conduction in intercalated layered crystalline solids

**Abstract**

As a generic property, all substances transfer heat through microscopic collisions of constituent particles1. A solid conducts heat through both transverse and longitudinal acoustic phonons, but a liquid employs only longitudinal vibrations2,3. As a result, a solid is usually thermally more conductive than a liquid. In canonical viewpoints, such a difference also serves as the dynamic signature distinguishing a solid from a liquid. Here, we report liquid-like thermal conduction observed in the crystalline AgCrSe2. The transverse acoustic phonons are completely suppressed by the ultrafast dynamic disorder while the longitudinal acoustic phonons are strongly scattered but survive, and are thus responsible for the intrinsically ultralow thermal conductivity. This scenario is applicable to a wide variety of layered compounds with heavy intercalants in the van der Waals gaps, manifesting a broad implication on suppressing thermal conduction. These microscopic insights might reshape the fundamental understanding on thermal transport properties of matter and open up a general opportunity to optimize performances of thermoelectrics.

**Disciplines**

Biological and Chemical Physics | Condensed Matter Physics | Materials Chemistry | Physical Chemistry | Thermodynamics

**Authors**

B. Li, H. Wang, Y. Kawakita, Q. Zhang, M. Feygenson, H. L. Yu, D. Wu, K. Ohara, T. Kikuchi, K. Shibata, T. Yamada, X. K. Ning, Y. Chen, J. Q. He, David Vaknin, R. Q. Wu, K. Nakajima, and M. G. Kanatzidis

# Liquid-like thermal conduction in intercalated layered crystalline solids

B. Li[1,*], H. Wang[2,*], Y. Kawakita[1], Q. Zhang[3], M. Feygenson[4], H. L. Yu[5], D. Wu[6], K. Ohara[7], T. Kikuchi[1], K. Shibata[1], T. Yamada[8], X. K. Ning[9], Y. Chen[5], J. Q. He[6,*], D. Vaknin[3], R. Q. Wu[2], K. Nakajima[1] and M. G. Kanatzidis[10,*]

[1]*J-PARC Center, Japan Atomic Energy Agency, Tokai, Ibaraki 319-1195, Japan.*

[2]*Department of Physics and Astronomy, University of California, Irvine, California 92697, USA.*

[3]*Ames Laboratory and Department of Physics and Astronomy, Iowa State University, Ames, Iowa 50011, USA.*

[4]*Jülich Center for Neutron Science, Forschungszentrum Jülich GmbH, D-52425, Jülich, Germany.*

[5]*Department of Mechanical Engineering, The University of Hong Kong, Pokfulam Road, Hong Kong SAR, China.*

[6]*Department of Physics, Southern University of Science and Technology (SUSTech), Shenzhen 518055, China.*

[7]*SPring-8, Japan Synchrotron Radiation Research Institute, Sayo, Hyogo 679-5198, Japan.*

[8]*Neutron Science and Technology Center, Comprehensive Research Organization for Science and Society (CROSS), Tokai, Ibaraki 319-1106, Japan.*

[9]*Hebei Key Lab of Optic-electronic Information and Materials, The College of Physics Science and Technology, Hebei University, Baoding 071002, China.*

[10]*Department of Chemistry, Northwestern University, Evanston, Illinois 60208, USA.*

*Corresponding authors. Email: bing.li@j-parc.jp (B. L.); huiw2@uci.edu (H. W.); he.jq@sustc.edu.cn (J. Q. H.); m-kanatzidis@northwestern.edu (M. G. K.).

**As a generic property, all substances transfer heat through microscopic collisions of constituent particles[1]. A solid conducts heat through both transverse and longitudinal acoustic phonons, but a liquid employs only longitudinal vibrations[2,3]. As a result, a solid is usually thermally more conductive than a liquid. In canonical viewpoints, such a difference also serves as the dynamic signature distinguishing a solid from a liquid. Here, we report liquid-like thermal conduction observed in the crystalline $AgCrSe_2$. The transverse acoustic (TA) phonons are completely suppressed by the ultrafast dynamic disorder while the longitudinal acoustic (LA) phonon is strongly scattered but survives, responsible for the intrinsically ultralow thermal conductivity. This scenario is applicable to a wide variety of layered compounds with heavy intercalants in the van der Waals gaps, manifesting broad implication on suppressing thermal conduction. These microscopic insights might reshape the fundamental understanding on thermal transport properties of matter and open up a general opportunity to optimize performances of thermoelectrics.**

Thermal transport is one of the most fundamental properties of matter[1]. As a persistent challenge, rationalizing anomalous thermal transport properties has been reforming our understanding on solid materials, such as the birth of phonon glasses[4-6] and the observation of wave-particle duality of phonon-transport in superlattices[7]. Meanwhile, materials with small thermal conductivity are desirable for a great diversity of applications like thermal insulation[8], optical phase-change memory devices[9], and efficient thermoelectric energy conversion[10]. Therefore, it is of both fundamental significance and technological interests to explore suppressed thermal transport in solids. By conducting a comprehensive study combining state-of-the-art neutron/X-ray scattering with density-functional-perturbation-theory (DFPT) calculations on the chalcogenide $AgCrSe_2$, we found the low-lying intense TA phonons that are exclusively dominated by motions of Ag atoms compete with fluctuations inherent in the order-to-disorder transition of Ag occupation. Phonons are significantly damped as temperature rises. Above the transition temperature, transverse vibrations of Ag atoms are suppressed by the ultrafast atomic fluctuations while the LA mode remains, characteristic of liquid-like thermal conduction with extremely low lattice thermal conductivity[11-13].

$AgCrSe_2$ crystallizes in a hexagonal structure with alternative Ag layers and $CrSe_6$ octahedral layers repeating along the *c* axis[14], as shown in **Fig. 1a**. Ag atoms lie in the equivalent tetrahedral

interstitial sites (I and II) in between $CrSe_6$ layers. The total energy calculations confirm this two-fold degenerate ground state (see Supplementary Section 1). These two sites form a buckled honeycomb lattice perpendicular to the *c* axis (lower panel of **Fig. 1b**). In the ground state, it is expected that only one specific site (here, let's distinguish as I) is fully occupied, as shown in the upper panel of **Fig. 1b**. As temperature rises, an increasing number of Ag ions immigrate to sites II owing to the jump diffusion. At $T_c$ of about 450 K, the occupation of Ag ions undergoes an order-to-disorder transition to the high-temperature phase with 50% occupation at each site while the space group of crystal symmetry changes from $R3m$ to $R\bar{3}m$. This transition is also regarded as a superionic transition due to the noticeable increase of ionic conduction[15]. The crystallographic changes are evidenced at X-ray scattering structure factor $S^X(Q)$ by the disappearance of Bragg peaks (003) and (006) as well as the weakening of $(10\bar{5})$, as shown in the inset of **Fig. 1c**. Neutron powder diffraction was used in tandem to track the evolution. The power-law fitting of the integrated intensity of the $(10\bar{5})$ Bragg peak gives rise to the critical exponent $\beta$ of 0.15 (Supplementary Figure 1), quite close to the theoretical value for the two-dimensional Ising model (0.125)[16].

At finite temperatures, the occupational disorder results in a strong diffuse scattering centered at about 2.0 $Å^{-1}$ (~ $Q_{100}$) (**Fig. 1c**). The diffuse scattering is understood in real space by Fourier-transforming $S^X(Q)$ into pair distribution function (PDF), $G^X(r)$ (details are given in Supplementary Section 2). Shown in **Fig. 2a** is $G^X(r)$ at selected temperatures. In the ordered crystal model, the first peak located at about 2.5 Å is the superposition of the nearest neighboring Cr-Se (octahedral coordination), Ag-Se (tetrahedral coordination), and Ag-Cr correlations. The second peak involves nearest neighboring Cr-Cr, Se-Se and Ag-Ag correlations, whose separations distribute around the lattice constant *a* (3.66339 Å at 341 K). In reality, however, the uniform nearest neighboring Ag-Ag distance splits into three sets due to the occupational disorder and the next nearest neighboring Ag-related correlations sequentially become diverse as well. This is responsible for the special temperature dependence of $G^X(r)$. With the guide of the partial PDF of Ag-related correlations shown in the lower part of **Fig. 2a**, it can be seen that heights of Ag-related peaks are much more susceptible to the change of temperature, such as those at 4.5, 13 and 19 Å (highlighted by vertical shaded bars). As a representative, the integrated intensity of the peak at 4.5 Å is plotted in **Fig. 2b**, which exhibits a well-defined

critical-like behavior, in contrast to the 3.5 Å peak where contributions of Ag-related pairs are marginal. Since the integrated intensity of a PDF peak is linked to the coordination number of associated pairs[17], the decreased intensity suggests that Ag-related pairs gradually lose their coordination with approaching the transition.

The experimental $G^X(r)$ is fitted to the $R3m$ crystal model. Shown in **Fig. 2c** is the comparison at 623 K. The discrepancies are found to be associated with Ag-related pairs. The model produces higher intensity because the actual disorder effect decreases the coordination. In this sense, the difference between this model and experimental data actually defines the degree of disorder, which is quantitatively evaluated by the goodness $R_w$ generated in the fitting. The temperature dependence of $R_w$ is obtained by applying similar fitting to data collected at other temperatures, as plotted in **Fig. 2d**. It stays around 0.14 at lower temperatures and tends to saturate after a steep growth in the vicinity of $T_c$. This is in agreement with the critical-like behavior of the integrated intensity shown in **Fig. 2b**. These observations together suggest the complete occupational disorder of Ag above $T_c$.

The thermally populated occupational disorder against the uniform long-range ordered structure manifests itself dynamically as the disorder-phonon coupling. Inelastic neutron scattering is an ideal approach in this aspect. The dynamic structure factor $S(Q,E)$ obtained at 5 K is plotted in **Fig. 3a** as a function of momentum transfer $Q$ and energy transfer $E$. Far away from the intense elastic line, there exist four less intense bands centered at about 3.5, 10, 13, and 18 meV (**Fig. 3c**). Note that the intensity spreading from $Q \sim 2.2$ Å$^{-1}$ and persisting up to 20 meV is attributed to magnons of $Cr^{3+}$ spins. To rationally assign these modes, the phonon dispersions (**Fig. 3b**) and phonon projected density of state (PDOS) (**Fig. 3d**) are calculated by using the DFPT approach. We identify that peaks at about 3.5, 10, 13, and 18 meV correspond to the energies of TA, LA, longitudinal optical (LO) and transverse optical (TO) modes, respectively. Dispersive-like intensity emanating from the Bragg peak (00$\underline{15}$) and ceasing at about 3.5 meV verifies that the mode of 3.5 meV is of acoustic phonons in nature (see Supplementary Fig. 8). Due to the lack of complete lattice dynamics calculations and high-resolution neutron data, Damay *et al.* assigned this mode to a local one[12]. Based on the PDOS, the phonon specific heat is also calculated as shown in **Fig. 3e**. It's worth noting that the TA phonons are exclusively dominated by motions of Ag (the integrated area of PDOS is about 91% of the total). This peculiar separation of partial PDOS is mainly attributed to two factors: the distinct masses of the constituent atoms and weak

bonding between Ag ions and Se across the van der Waals gap. Further systematical calculations on $A$CrSe$_2$ system ($A$ = Li, Ag and Cs) in the layered $R3m$ and $P\bar{3}m1$ structures clearly verify that heavy intercalants predominantly contribute to low-energy TA phonons (**Fig. 3f**).

Now, we turn our attention to the dynamic aspect of the diffuse scattering. **Fig. 4a** and **b** show $S(Q,E)$ with incident energy ($E_i$) of 5.931 meV at 150 and 520 K, respectively. It can be seen that pronounced diffuse scattering exists at $Q \sim 2.0$ Å$^{-1}$. At 150 K, the diffuse scattering appears just in the vicinity of the elastic line and TA phonons are fairly sharp. Nevertheless, the diffuse scattering becomes dominant at 520 K at the expense of Bragg peaks and TA phonons. Their evolution as a function of temperature is plotted in **Fig. 4c**. TA phonons are softened and gradually merged into the diffuse scattering around $T_c$. The complete suppression of TA phonons is confirmed in the higher $Q$ region where there is fewer component of the diffuse scattering (see Supplementary Fig. 8). The spectral fitting yields the linewidth ($\Gamma_{TA}$ and $\Gamma_{Diffuse}$) as summarized in **Fig. 4d**. $\Gamma_{TA}$ exhibits a rapid increase as approaching $T_c$ while the temperature dependence of $\Gamma_{Diffuse}$ is characteristic of a critical-like change. Around $T_c$, their comparable timescales facilitate the extreme dynamic competition so that TA phonons are suppressed. Such robust atomic fluctuations are the atomic-level origin of large ionic conductivity even below $T_c$[15]. Differing from its strong temperature dependence, $\Gamma_{Diffuse}$ is nearly $Q$ independent at a given temperature, indicating its local nature.

Do the TA phonons collapse into localized transverse oscillators above $T_c$? To answer this question, it is crucial to compare the characteristic timescales of the system. We take the highest frequency of TA phonons (3.5 meV) as the cut-off frequency of possible local oscillators[18]. It corresponds to a period of about 1.2 ps, which is much longer than the relaxation time ($1/\Gamma_{Diffuse}$) of dynamic disorder, ~ 0.4 ps. As a result, the transverse vibrations cannot complete because Ag atoms attempting to transversely vibrate wouldn't return back to their initial positions[2,3]. Moreover, the specific heat of the lattice subsystem tends to decrease down to below 3$R$ ($R$ is the gas constant) just above $T_c$ as shown in **Fig. 3e**. This supports the occurrence of the liquid-like behavior as a liquid ideally has specific heat of 2$R$ per mole-atom due to losing of the transverse vibration degree of freedom[2,3]. Consequently, the thermal conduction is solely contributed by the LA phonons above $T_c$ (see Supplementary Section 5). The liquid-like thermal conduction discovered in AgCrSe$_2$ emerges as a unpreceded approach for tuning thermal transport of matter,

beyond the conventional ideas such as anharmonic phonon interacitons[19-21], uncorrelated or concerted rattling modes[4-6,22], interfaces and other defects[23,24], not only because of the lost transverse vibrations, but also the strong disorder scattering of the LA phonon at similar timescales. Recently, it is assumed that the superionic behavior of Cu in $Cu_2Se$ might dismiss transverse modes[25], but the inelastic neutron scattering study suggests the dynamics of Cu ions is too slow to affect phonons[26].

The liquid-like thermal conduction is a promising general strategy for the suppression of thermal conduction given that the selective disorder-phonon coupling is translational to layered compounds intercalated with heavier atoms. The weak coupling across the van der Waals gaps ensures that the motions of heavy intercalants dominate TA phonons. Structurally, the intercalated atoms can occupy either tetrahedral, octahedral or trigonal prismatic interstitial sites[27]. In the first case, as shown in **Fig. 1b**, long-range ordered ground states are verified to exist, either as a triangle-lattice *ferromagnet* ($AgCrSe_2$ case) or as a honeycomb-lattice *antiferromagnet*[28]. Atomic fluctuations are expected to completely suppress TA phonons when order-to-disorder transitions take place. Hence, as long as the heavy intercalants occupy tetrahedral interstitial sites, the liquid-like thermal conduction is anticipated. Even though the occupational order is inactive for the last two cases (fully filled triangle lattice), taking $AgCrSe_2$ as an example, our calculations indicate that it is feasible to switch the octahedral to tetrahedral occupation by applying uniaxial stresses along the *c* direction, as depicted in **Fig. 5a**. The calculated energy landscape is characteristic of a reentrant octahedral occupation with critical stresses of -2.4/+2.7 GPa. The phase stability at high stresses is further confirmed by absence of imaginary frequencies in the phonon dispersion (Supplementary Fig. 5). More specifically, we structurally explore the candidates based on the general formula $A^{+}TM^{3+}X^{2-}_2$ with given oxidation states using the data-mined ionic substitution method, where *A* represents Ag as well as heavier In and Tl, TM is 3d transition metals except Zn, and X is S and Se. It can be seen in **Fig. 5b** that several compounds have quite high probabilities of crystallizing in *R*3*m* structure in which the heavier atoms occupy tetrahedral interstitials so that they are candidates undergoing liquid-like thermal conduction. Indeed, the $AgCrS_2$[29] and $AgNiSe_2$[30] have been found to crystallize in this structure.

In summary, we observe liquid-like thermal conduction in the crystalline $AgCrSe_2$, and unveil the intimate competition between the dynamic disorder and TA phonons as the microscopic

origin in nature. Being of fundamental significance, the scenario of liquid-like thermal conduction is potentially a general route to suppressed thermal conductivity of solids, especially intercalated layered compounds.

**References:**


1. Tritt, T. M. *Thermal conductivity: theory, properties, and applications* (Klumer Academic/Plenum Publishers, 2004).
2. Frenkel, J. *Kinetic theory of liquids* (Oxford Univ. Press, 1947).
3. Trachenko, K. & Brazhkin, V. V. Collective modes and thermodynamics of the liquid state. *Rep. Prog. Phys.* **79**, 016502 (2016).
4. Slack, G. A. in *CRC Handbook of Thermoelectrics* (ed. Rowe, M.) 407–440 (CRC, 1995).
5. Keppens, V. *et al*. Localized vibrational modes in metallic solids. *Nature* **395**, 876–878 (1998).
6. Christensen, M. *et al*. Avoided crossing of rattler modes in thermoelectric materials. *Nat. Mater.* **7**, 811–815 (2008).
7. Ravichandran, J. *et al*. Crossover from incoherent to coherent phonon scattering in epitaxial oxide superlattices. *Nat. Mater.* **13**, 168–172 (2014).
8. Padture, N. P., Gell, M. & Jordan, E. H. Thermal barrier coatings for gas-turbine engine applications. *Science* **296**, 280–284 (2002).
9. Siegrist, T., Merkelbach, P. & Wuttig, M. Phase change materials: challenges on the path to a universal storage device. *Annu. Rev. Condens. Matter Phys.* **3**, 215–237 (2012).
10. Bell, L. E. Cooling, heating, generating power, and recovering waste heat with thermoelectric systems. *Science* **321**, 1457–1461 (2008).
11. Gascoin, F. & Maignan, A. Order–disorder transition in $AgCrSe_2$: a new route to efficient thermoelectrics. *Chem. Mater.* **23**, 2510–2513 (2011).
12. Damay, F. *et al*. Localised Ag(+) vibrations at the origin of ultralow thermal conductivity in layered thermoelectric $AgCrSe_2$. *Sci. Rep.* **6**, 23415 (2016).
13. Wu, D. *et al*. Revisiting $AgCrSe_2$ as a promising thermoelectric material. *Phys. Chem. Chem. Phys.* **18**, 23872–23878 (2016).

14. Van Der Lee, A. & Wiegers, G. A. Anharmonic thermal motion of Ag in $AgCrSe_2$: A high-temperature single-crystal X-ray diffraction study. *J. Solid State Chem.* **82**, 216–224 (1989).

15. Murphy, D. W. & Chen, H. S. Superionic conduction in $AgCrS_2$ and $AgCrSe_2$. *J. Electrochem. Soc.* **124**, 1268–1271 (1977).

16. Onsager, L. Crystal Statistics. I. A two-dimensional model with an order-disorder transition. *Phys. Rev.* **65**, 117–149 (1944).

17. Louca, D. & Egami, T. Local lattice distortions in $La_{1-x}Sr_xMnO_3$ studied by pulsed neutron scattering. *Phys. Rev. B* **59**, 6193–6204 (1999).

18. Cahill, D. G., Watson, S. K. & Pohl, R. O. Lower limit to the thermal conductivity of disordered crystals. *Phys. Rev. B* **46**, 6131 (1992).

19. Delaire, O. *et al*. Giant anharmonic phonon scattering in PbTe. *Nat. Mater.* **10**, 614–619 (2011).

20. Zhao, L. D. *et al*. Ultralow thermal conductivity and high thermoelectric figure of merit in SnSe crystals. *Nature* **508**, 373–377 (2014).

21. Li, C. W. *et al.* Orbitally driven giant phonon anharmonicity in SnSe. *Nat. Phys.* **11**, 1063–1069 (2015).

22. Lin, H. *et al*. Concerted Rattling in $CsAg_5Te_3$ leading to ultralow thermal conductivity and high thermoelectric performance. *Angew. Chem. Int. Ed.* **55**, 11431–11436 (2016).

23. Minnich, A. J., Dresselhaus, M. S., Ren, Z. F. & Chen, G. Bulk nanostructured thermoelectric materials: current research and future prospects. *Energy Environ. Sci.* **2**, 466–479 (2009).

24. Kim, S. I. *et al*. Dense dislocation arrays embedded in grain boundaries for high-performance bulk thermoelectrics. *Science* **348**, 109–114 (2015).

25. Liu, H. *et al*. Copper ion liquid-like thermoelectrics. *Nat. Mater.* **11**, 422–425 (2012).

26. Voneshen, D. J., Walker, H. C., Refson, K. & Goff, J. P. Hopping time scales and the phonon-liquid electron-crystal picture in thermoelectric copper selenide. *Phys. Rev. Lett.* **118**, 145901 (2017).

27. Hibma, T. in *Intercalations Chemistry* (ed. Whittingham, M. S. & Jacobson, A. J.) 285–313 (Academic Press, 1982).

28. Subbaswamy, K. R. & Mahan, G. D. Renormalization group results for lattice-gas phase boundaries in two dimensions. *Phys. Rev. Lett.* **37**, 642 (1976).

29. Brüesch, P., Hibma, T. & Bührer, W. Dynamics of the two-dimensional superionic conductor $AgCrS_2$, *Phys. Rev. B* **27**, 5052–5061 (1983).

30. Aliev, M. I. *et al.*, Production and X-ray studies of $AgCrSe_2$, $AgCrTe_2$, $AgNiSe_2$ and $AgNiTe_2$ compounds. *Doklady Akademii Nauk Azerbajdzhanskoj SSR* 13, 42–46 (1981).

## Methods

### Sample preparation

The powder samples were prepared using solid state reaction method. The starting materials Ag, Cr and Se powder in the ratio of stoichiometric composition were ground, mixed, and pelletized. The pellets were sealed in evacuated quartz tubes. The tubes were placed in a box furnace and heated first to 473 K for 6 hours, and then to 1173 K for 24 hours, followed by the natural cooling to room temperature. Before all neutron scattering and X-ray scattering measurements, the samples were annealed under argon flow at 523 K overnight.

### Specific heat measurements

The specific heat capacity at constant pressure ($C_p$) was measured using a differential scanning calorimetry (DSC) (Netzsch STA449, Germany) above room temperature. A Quantum Design Physical Properties Measurement System (PPMS) was used to measure $C_p$ in the temperature region of 5 – 320 K. The specific heat at constant volume ($C_v$) is obtained by subtracting contributions of lattice dilation and electrons (see Supplementary Section 4).

### Neutron powder diffraction

The neutron powder diffraction measurements were performed at the Nanoscale Ordered Materials Diffractometer (NOMAD) in Spallation Neutron Source of Oak Ridge National Laboratory, USA[31]. Constant temperature scans were taken at several temperatures with a vacuum furnace. Each scan took about 1 hour. An empty vanadium can, a standard vanadium rod, and the background were also measured at room temperature for pair distribution function (PDF) analysis. The diffraction data was analyzed using the Rietveld refinement method in GSAS[32,] which are described in Supplementary Section 1 in detail.

### Synchrotron X-ray powder scattering

The high energy X-ray powder scattering was carried out at the beam line BL04B2 of SPring-8, Japan, with photon energy of 113 keV[33]. About 0.2 gram powder was sealed under helium gas into a quartz capillary. The constant temperature scans were taken in the vicinity of the order-to-disorder transition. Each scan took about 3.5 hours. An empty capillary sealed under helium gas was also measured at room temperature as a reference. X-ray pair distribution function (PDF), $G^X(r)$, is obtained by Fourier transforming the normalized structure factor $S^X(Q)$ with cutoff ($Q_{max}$) of about 25 $Å^{-1}$, after subtraction of the background (the empty capillary) and the Compton scattering. The integrated intensities of $G^X(r)$ peaks were determined by fitting to multiple Gaussian functions. All $G^X(r)$ patterns were refined using PDFgui[34] with the structural model of $R3m$ in the region of [1, 20] Å.

### Inelastic neutron scattering

Multi-$E_i$ time-of-flight inelastic neutron scattering measurements were performed at the cold neutron disk chopper spectrometer BL14 AMATERAS of J-PARC in Japan[35]. The powder sample around 7 grams was sealed in an aluminum can with indium wire. A cryostat was used to access lower temperatures and a niobium furnace was used for higher temperatures measurements. The chopper configurations were set to select $E_i$ of 23.71, 10.542, 5.931 and 2.635 meV at the low-resolution (LR) mode while 23.71, 5.931 and 2.635 meV at high-resolution (HR) mode[36]. The data reduction was completed using Utsusemi suite[37]. The background contributed by the niobium furnace was subtracted. The resulted $S(Q,E)$ data was visualized in Mslice of DAVE[38]. The $Q$-cutting spectra were fitted in PAN of DAVE by including a damped harmonic oscillator function[39], a Lorentzian function, a delta function, and a constant background, which are convoluted to the instrumental resolution. They describe the transverse acoustic phonons, dynamic diffuse scattering, incoherent elastic scattering, and background, respectively.

**First-principles calculations**

Density functional theory (DFT) calculations were performed with the Vienna Ab-initio Simulation Package (VASP)[40]. The generalized gradient approximation (GGA) in the Perdew-Burke-Ernzerhof (PBE)[41] form and the projector-augmented wave method (PAW)[42,43] was applied in all DFT calculations. The energy cutoff for the plane-wave expansion was 500 eV, and Brillouin zone was sampled adopting the Γ-centered Monkhorst-Pack method with a density of about $2\pi \times 0.03$ Å$^{-1}$ [44]. Spin-orbital coupling (SOC) was not treated in the simulation given that SOC of Ag, Cr and Se is not strong and has a minimal effect on lattice vibration[45]. Calculations were carried out on a 4×4×4 supercell containing 256 atoms to obtain the collective vibrational spectra of phonons by using Phonopy[46]. The uniaxial stress was applied by varying $c$ axis step by step with in plane lattice constant and atomic position fully relaxed. Structures were optimized with a criterion that the atomic force on each atom becomes weaker than 0.01 eV/Å and the energy convergence is better than $10^{-8}$ eV. Similar procedures were applied to $LiCrSe_2$ and $CsCrSe_2$.

**Lattice-dynamics calculations**

Density functional perturbation theory (DFPT) is a particularly powerful and flexible theoretical technique that allows calculation of electron-density linear response within the density functional framework, thereby facilitating the acquisition of vibrational frequencies within crystalline materials[47]. Lattice dynamics calculations were carried out using the Phonopy package[46], with VASP employed as the calculator to obtain interatomic force constants (IFCs) via a DFPT calculation. To balance the accuracy and computational efforts, we calculated the phonon spectra based on the ferromagnetic structure, given that energy difference between ferromagnetic and antiferromagnetic is very small (1~2 μeV/atom). During post-processing, sampling the phonon frequencies on a 30×30×30 centered q mesh converged the vibrational density of states, and hence the values of thermodynamic properties were calculated from it. For the quasi-harmonic approximation (QHA) calculations[46], additional finite displacement calculations were performed on unit cells at approximately ±2% of the equilibrium volume in steps of 0.5%, which guarantee these volumes correspond to temperatures inside the validity range for the QHA.

**Data-mined ionic substitution structural prediction**

The structure predictor module in the Materials Project was used to explore the crystal structures at given composition of $A^+TM^{3+}X^{2-}{}_2$ and oxidation states[48,49]. Atom $A$ is chosen to be Ag and heavier Tl and In; TM is 3d transition metals except Zn; and X is S and Se. The probability of $R3m$ structure is normalized to that of most-probable-phase for each composition.

**Data availability**

The data that support the findings of this study are available from the corresponding authors on request.


31. Neuefeind, J., Feygenson, M., Carruth, J., Hoffmann, R. & Chipley K. K. The nanoscale ordered materials diffractometer NOMAD at the spallation neutron source. *Nucl. Instrum. Methods Phys. Res., Sect. B* **287**, 68–75 (2012).

32. Toby, B. H. EXPGUI, a graphical user interface for GSAS, *J. Appl. Cryst.* **34**, 210–213 (2001).

33. Isshiki, M., Ohishi, Y., Goto, S., Takeshita, K. & Ishikawa T. High-energy X-ray diffraction beamline: BL04B2 at SPring-8. *Nucl. Instrum. Methods Phys. Res., Sect. B* **476**–**478**, 663–666 (2012).

34. Farrow, C. L. PDFfit2 and PDFgui: computer programs for studying nanostructure in crystals, *J. Phys.: Condens. Matter* **19**, 335219 (2007).

35. Nakajima, K. *et al.* AMATERAS: a cold-neutron disk chopper spectrometer. *J. Phys. Soc. Jpn.* **80**, SB028 (2011).

36. Nakamura, M. *et al.* First demonstration of novel method for inelastic neutron scattering measurement utilizing multiple incident energies. J. Phys. Soc. Jpn. **78**, 093002 (2009).

37. Inamura, Y., Nakatani, T., Suzuki, J. & Otomo, T. Development status of software "Utsusemi" for chopper spectrometers at MLF, J-PARC. *J. Phys. Soc. Jpn.* **82**, SA031 (2013).

38. Azuah, R. T. *et al.* DAVE: A comprehensive software suite for the reduction, visualization, and analysis of low energy neutron spectroscopic data, *J. Res. Natl. Inst. Stan. Technol.* **114**, 341 (2009).

39. Fåk, B. & Dorner, B. Phonon line shapes and excitation energies. *Physica B* **234–236**, 1107–1108 (1997).

40. Kresse, G. & Hafner, J. Ab initio molecular-dynamics simulation of the liquid-metal amorphous-semiconductor transition in germanium. *Phys. Rev. B* **49**, 14251–14269 (1994).

41. Perdew, J. P., Burke K. & Ernzerhof, M. Generalized gradient approximation made simple. *Phys. Rev. Lett.* **77**, 3865 (1996).

42. Kresse, G. & Joubert, D. From ultrasoft pseudopotentials to the projector augmented-wave method. *Phys. Rev. B* **59**, 1758 (1999).

43. Blöchl, P. E. Projector augmented-wave method. *Phys. Rev. B* **50**, 17953 (1994).

44. Monkhorst H. J. & Pack, J. D. Special points for Brillouin-zone integrations. *Phys. Rev. B* **13**, 5188 (1976).

45. Romero, A. H. *et al.* Lattice properties of PbX (X = S,Se,Te): Experimental studies and ab initio calculations including spin-orbit effects. *Phys. Rev. B* **78**, 224302 (2008).

46. Togo, A., Oba, F. & Tanaka, I. First-principles calculations of the ferroelastic transition between rutile-type and $CaCl_2$-type $SiO_2$ at high pressures. *Phys. Rev. B* **78**, 134106 (2008).

47. Baroni, S., de Gironcoli, S., Dal Corso, A. & Giannozzi, P. Phonons and related crystal properties from density-functional perturbation theory. *Rev. Mod. Phys.* **73**, 515–562 (2001).

48. Jain, A. *et al.* The Materials Project: A materials genome approach to accelerating materials innovation. *APL Mater* **1**, 011002 (2013).

49. Hautier, G., Fischer, C., Ehrlacher, V., Jain, A. & Ceder, G. Data mined ionic substitutions for the discovery of new compounds. *Inorg. Chem.* **50**, 656–663 (2011).

**Acknowledgment** We acknowledge the award of beam time from Spallation Neutron Source, a DOE office of Science User Facility operated by the Oak Ridge National Laboratory, via proposal IPTS-13971, from SPring-8 via proposal No. 2015B1070, and from J-PARC via proposal No. 2012P0906. H.W. and R.Q.W. were supported by DOE-BES (Grant No. DE-FG02-05ER46237) and the computer simulations were supported by National Energy Research Scientific Computing Center (NERSC). Ames Laboratory is operated for the U.S. Department of Energy by Iowa State University under Contract No. DE-AC02-07CH11358. D.W. and J.Q.H.

were supported by the Natural Science Foundation of Guangdong Province (Grant No. 2015A030308001) and the leading talents of Guangdong Province Program (Grant No. 00201517). H.L.Y. and Y.C. acknowledge the research computing facilities offered by ITS, HKU. We thank Dr. M. Kofu for the fruitful discussion.

**Author contributions** B.L. and H.W. planned the project. Q.Z., D.V., D.W., and J.Q.H. synthesized the samples. D.W. and J.Q.H. carried out thermoelectric measurements. X.K.N. measured the low-temperature specific heat and did transmission electron microscopy observation. M.F. performed neutron powder diffraction measurements. B.L., Y.K., and K.O. collected X-ray scattering data. B.L., Y.K., T.K., K.S., T.Y., and K.N. performed inelastic neutron scattering measurements. H.W., H.L.Y., Y.C., and R.Q.W. performed theoretical calculations. B.L., H.W., J.Q.H., and M.G.K. interpreted all results and wrote the manuscript with discussion and input from all the coauthors.

**Additional information** Supplementary information is available in the online version of the paper. Reprints and permissions information is available online at www.nature.com/reprints. Correspondence and requests for materials should be addressed to corresponding authors.

**Competing financial interests** The authors declare no competing financial interests

**Figure 1**. **Structures and phase transition. a**, The crystal structure of $AgCrSe_2$ with the $CrSe_6$ octahedra and $AgSe_4$ tetrahedra highlighted. There are two equivalent sites for Ag (I and II), whose occupations $p$(I) and $p$(II) are dependent on temperature. The phase transition is driven from $R3m$ to $R\bar{3}m$ when $p$(I) = $p$(II) at $T_c$. **b**, The occupational orders of tetrahedral interstitial sites. The uniform occupation leads to a "ferromagnetic" ground state (upper panel), such as $AgCrSe_2$, compared with an "antiferromagnetic" one at random occupation (lower panel). **c**, The structure factor, $S^X(Q)$, obtained in X-ray scattering at 308 and 623 K. The diffuse scattering appears at the scattering vector of Ag-lying {100} planes, about 2.0 $Å^{-1}$. The inset highlights $S^X(Q)$ at small $Q$ region for temperature evolution (upper) and two end temperatures (lower). Bragg peaks of (003), (006) and $(10\bar{5})$ are labelled. The transition temperature $T_c$ is marked at the temperature where the (003) Bragg peak tends to disappear.

**Figure 2. Thermally populated occupational disorder of Ag atoms. a**, The experimental X-ray PDF, $G^{X}(r)$, obtained from X-ray scattering at selected temperatures up to 20 Å (for the comparison with neutron case, see Supplementary Section 2). Underneath is the superposition of partial $G^{X}(r)$ for Ag-involved pairs (Ag-Ag, Ag-Cr and Ag-Se) calculated on the *R*3*m* crystal model. **b**, The integrated intensity of $G^{X}(r)$ for Ag-correlation-poor peak at 3.5 Å and Ag-correlation-rich peak at 4.5 Å, which are labelled by a circle and a square in **a**, respectively. **c**, The real-space refinement of experimental $G^{X}(r)$ based on the *R*3*m* crystal model at 623 K. **d**, The goodness of this real-space refinement as a function of temperature. The vertical shaded bars in **a** and **c** highlight the positions where Ag-related correlations are dominant. In **b** and **d** $T_c$ is marked by a dash line.

**Figure 3. Experimental and theoretical results of phonons. a**, The contour plot of dynamic structure factor $S(Q,E)$ obtained in inelastic neutron scattering with incident neutron energy $E_i$ = 23.71 meV in the low-resolution (LR) mode at 5 K. **b**, The calculated phonon dispersion relationship by using DFPT quasi-harmonic approximation (QHA) method. The color bar depicts the magnitude of isotropic volumetric expansions that result in the monotonous softening of all modes. **c**, The constant-$Q$ cuts of $S(Q,E)$ obtained at $E_i$ = 23.71 meV in the high-resolution (HR) mode in the interval of [3,4] $Å^{-1}$, where peaks correspond to energies of TA, LA, LO and TO modes. **d**, Calculated PDOS of $AgCrSe_2$. **e**, Specific heat under constant volume that becomes smaller than the DFT value as well as 3*R* above $T_c$ (*R* is the gas constant). **f**, The integrated-area ratio between the partial PDOS of *A* and total PDOS for TA phonons of $ACrSe_2$ in *R*3*m* and $P\bar{3}m1$ structures, where *A* = Li, Ag, and Cs.

**Figure 4. Suppression of TA phonons. a**,**b**, $S(Q,E)$ surface plots at 150 and 520 K at $E_i$ = 5.931 meV in the HR mode. **c**, Contour plot of $S(Q,E)$ as a function of temperature with $E_i$ = 10.542 meV in the LR mode at $Q$ of [2.5, 3] $Å^{-1}$. **d**, The half-width-at-half-maximum of the TA phonons and the diffuse scattering determined in spectral fitting. $Q$-dependence of the latter is shown in the inset. The squares and circles are data points obtained in LR and in HR modes, respectively. The dash lines are guide for eyes. $T_c$ is labelled in both **c** and **d**.

**Figure 5. Controllable occupational orders in $A^{+}TM^{3+}X^{2-}_{2}$. a**, Total energy barriers of $AgCrSe_2$ in $R3m$ phase with Ag in tetrahedral interstitial sites and in $P\bar{3}m1$ phase with Ag in octahedral interstitial sites as a function of uniaxial stresses applied along the *c* direction. The inset demonstrates the atomic slabs in $R3m$ phase and $P\bar{3}m1$ phase. The dotted lines show the phase boundaries. **b**, predicted probabilities of $R3m$ phase normalized to the probability of the most-probable-phase. Here, $A$ = Ag, In and Tl, TM = 3d transition metals except Zn, X = S, Se.

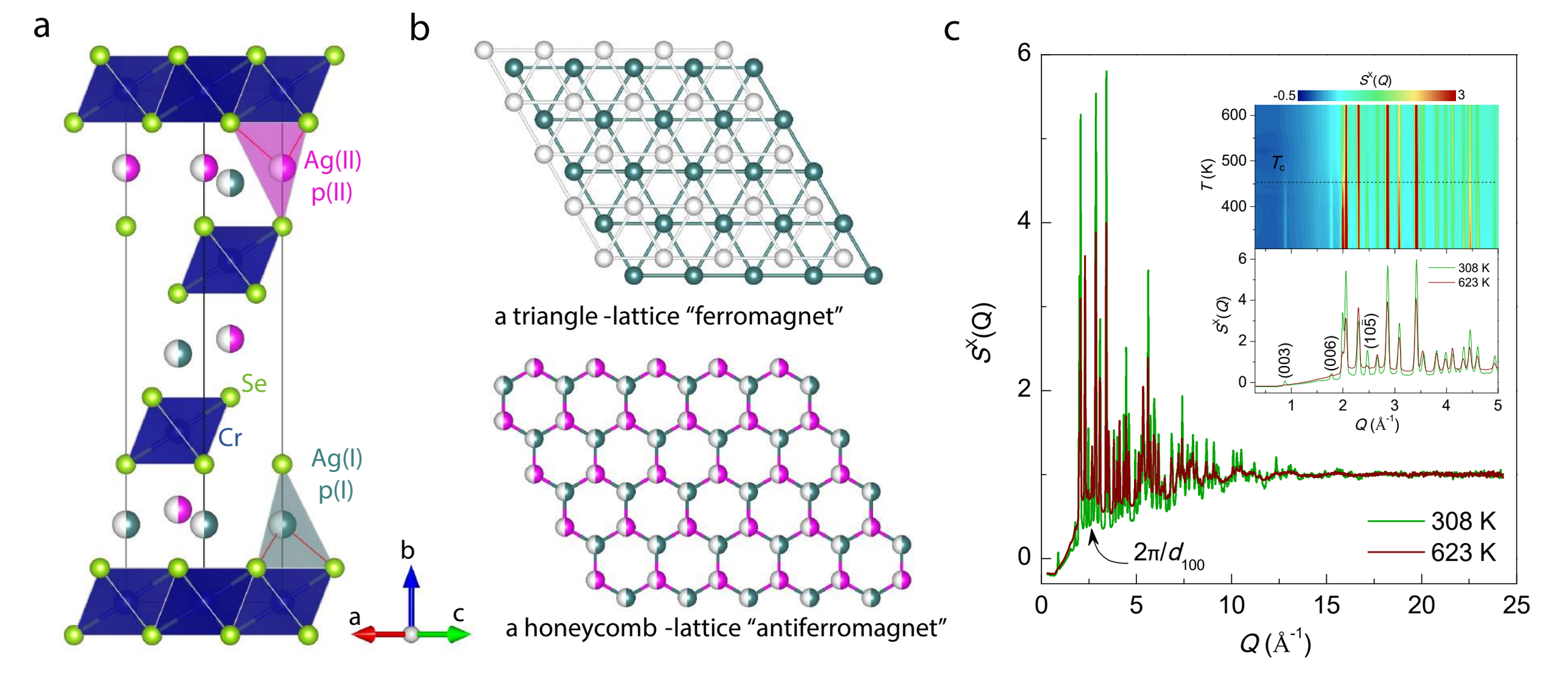
a
Ag(II)
p(II)
Se
Cr
Ag(I)
p(I)
b
a
c
b
a triangle -lattice “ferromagnet”
a honeycomb -lattice “antiferromagnet”
c
$S^x(Q)$
$Q$ (Å$^{-1}$)
$2\pi/d_{100}$
308 K
623 K
$S^x(Q)$
-0.5
3
$T$ (K)
$T_c$
(003)
(006)
(105)

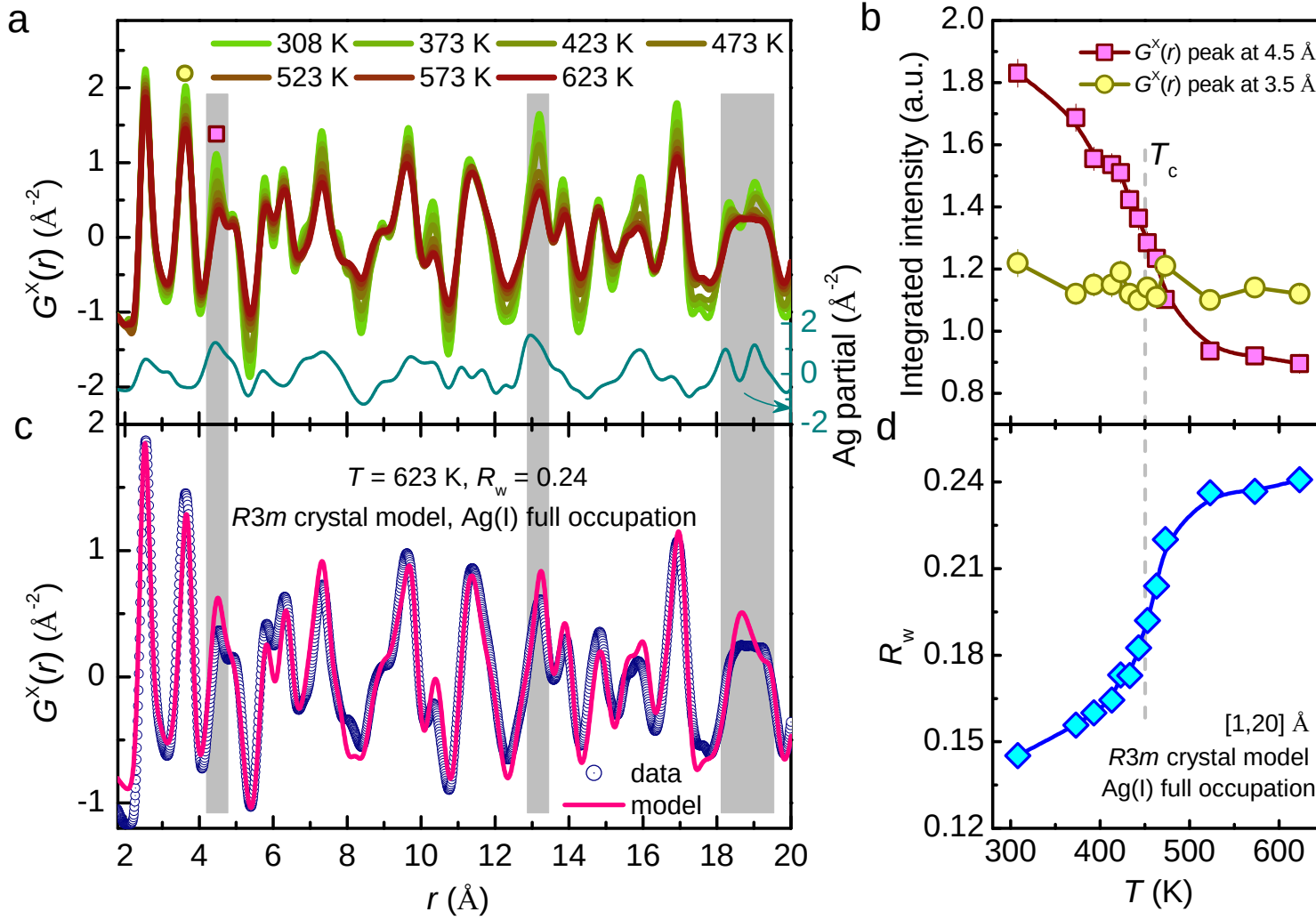
a
308 K
373 K
423 K
473 K
523 K
573 K
623 K
$G^X(r)$ (Å$^{-2}$)
Ag partial (Å$^{-2}$)
b
$G^X(r)$ peak at 4.5 Å
$G^X(r)$ peak at 3.5 Å
$T_c$
Integrated intensity (a.u.)
c
$T$ = 623 K, $R_w$ = 0.24
$R3m$ crystal model, Ag(I) full occupation
data
model
$r$ (Å)
d
$R_w$
[1,20] Å
$R3m$ crystal model
Ag(I) full occupation
$T$ (K)

a

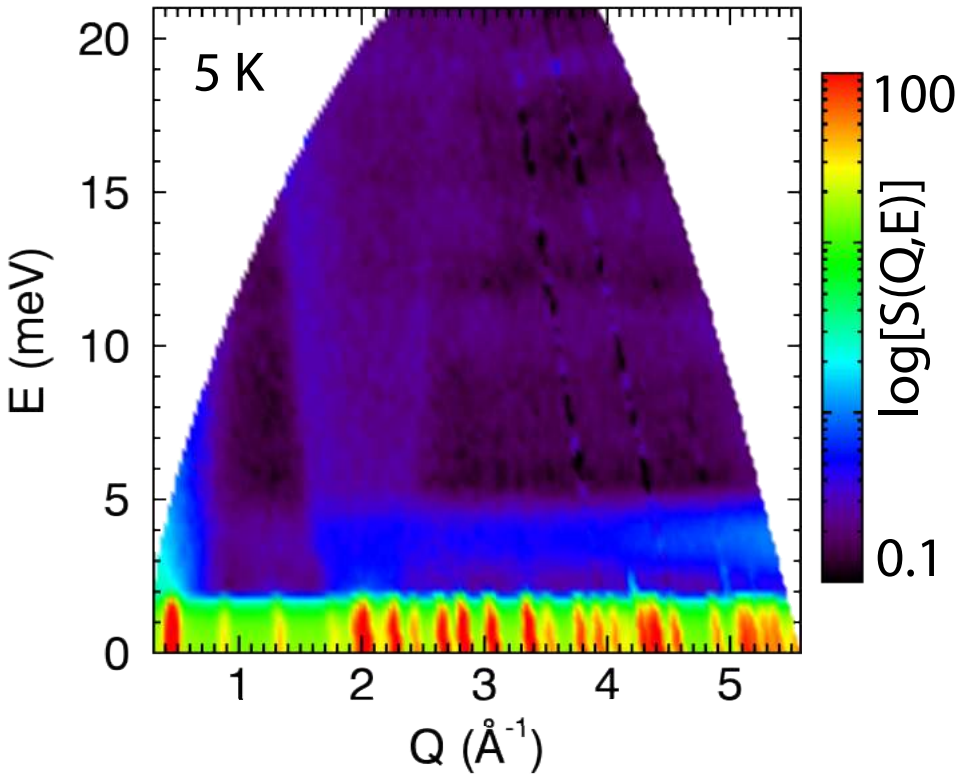
5 K
E (meV)
Q (Å$^{-1}$)
log[S(Q,E)]
100
0.1

b

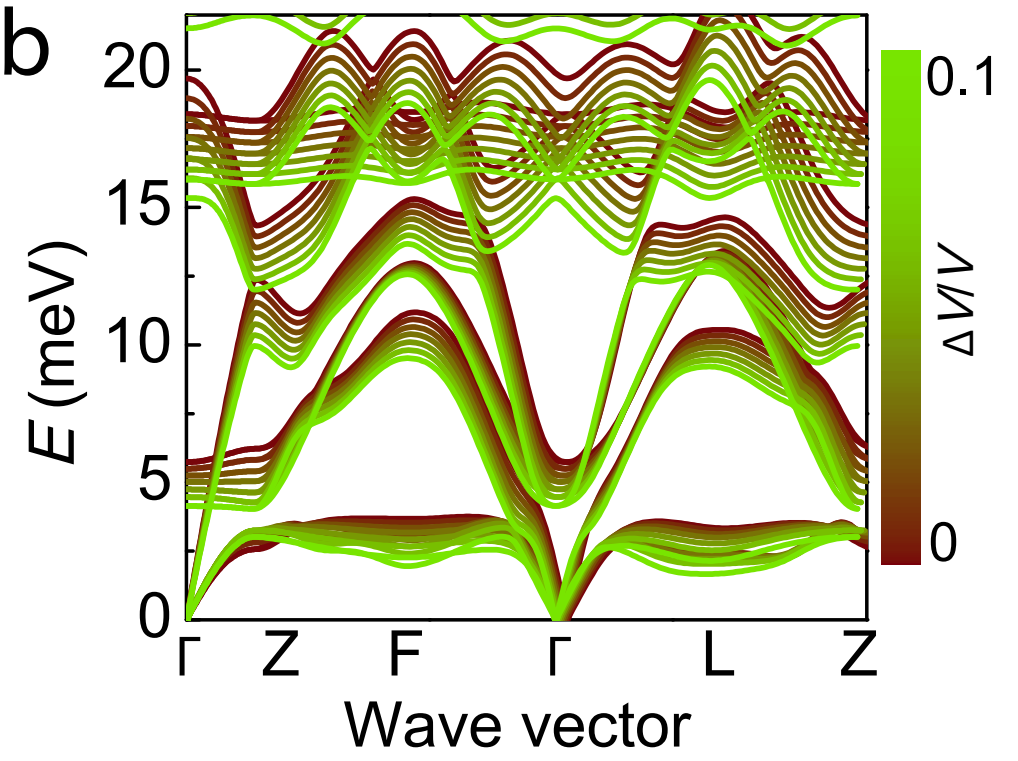
E (meV)
Γ Z F Γ L Z
Wave vector
ΔV/V
0.1
0

c

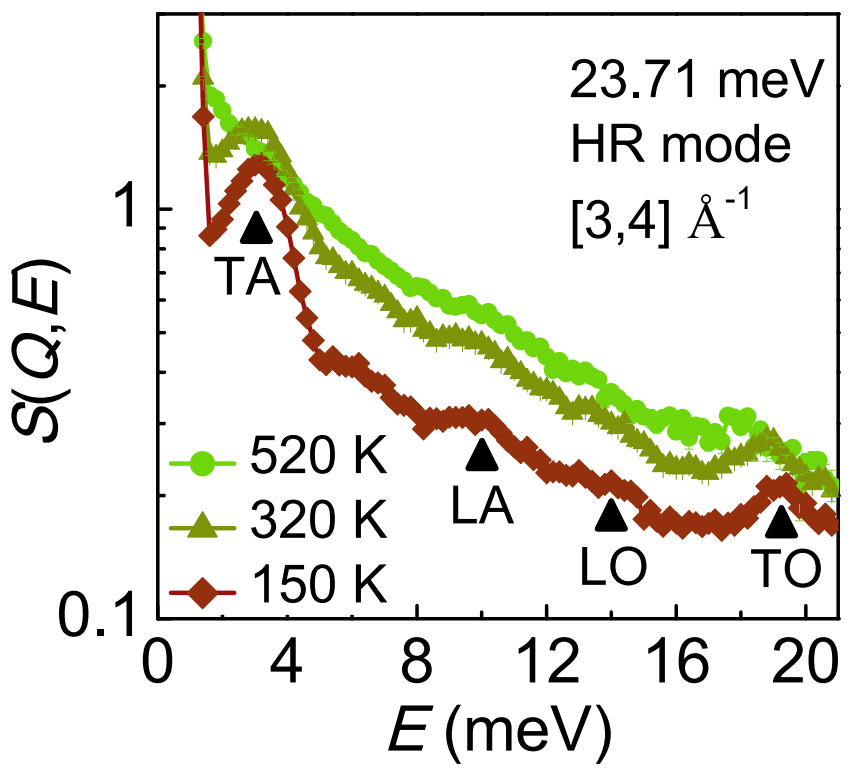
23.71 meV
HR mode
[3,4] Å$^{-1}$
TA
LA
LO
TO
520 K
320 K
150 K
S(Q,E)
E (meV)

d

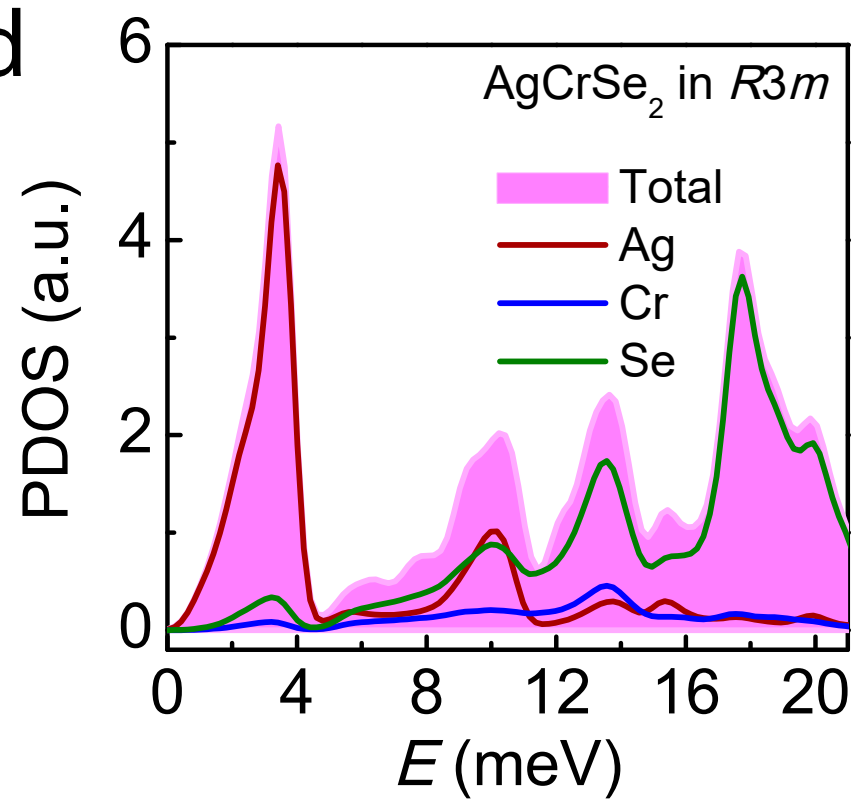
AgCrSe$_2$ in R3m
Total
Ag
Cr
Se
PDOS (a.u.)
E (meV)

e

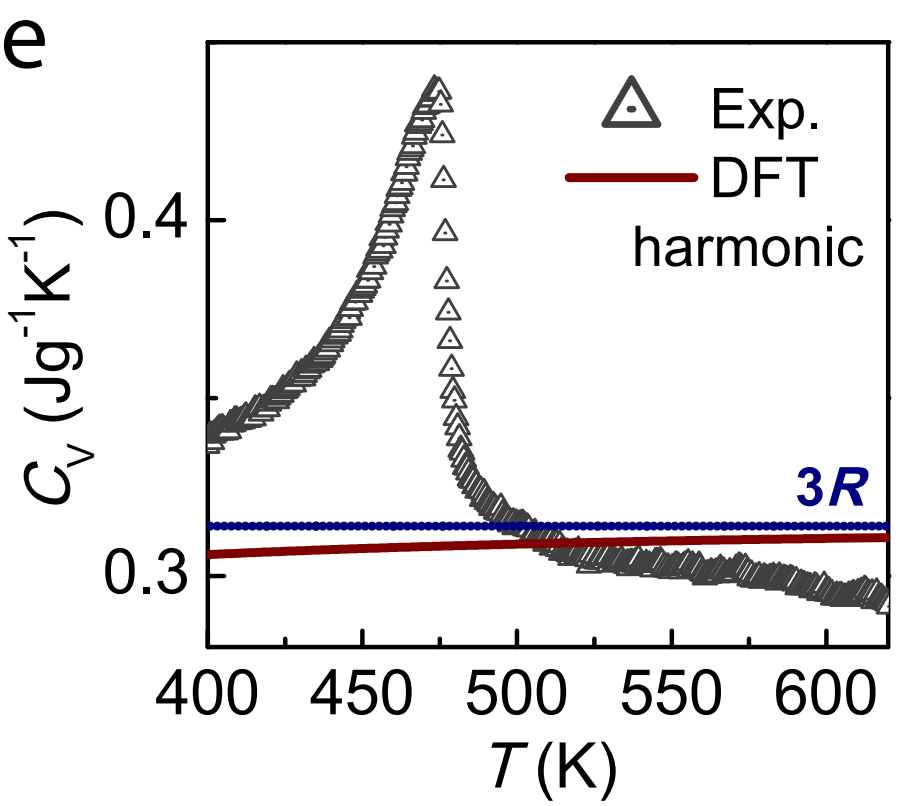
Exp.
DFT
harmonic
3R
C$_V$ (Jg$^{-1}$K$^{-1}$)
T (K)

f

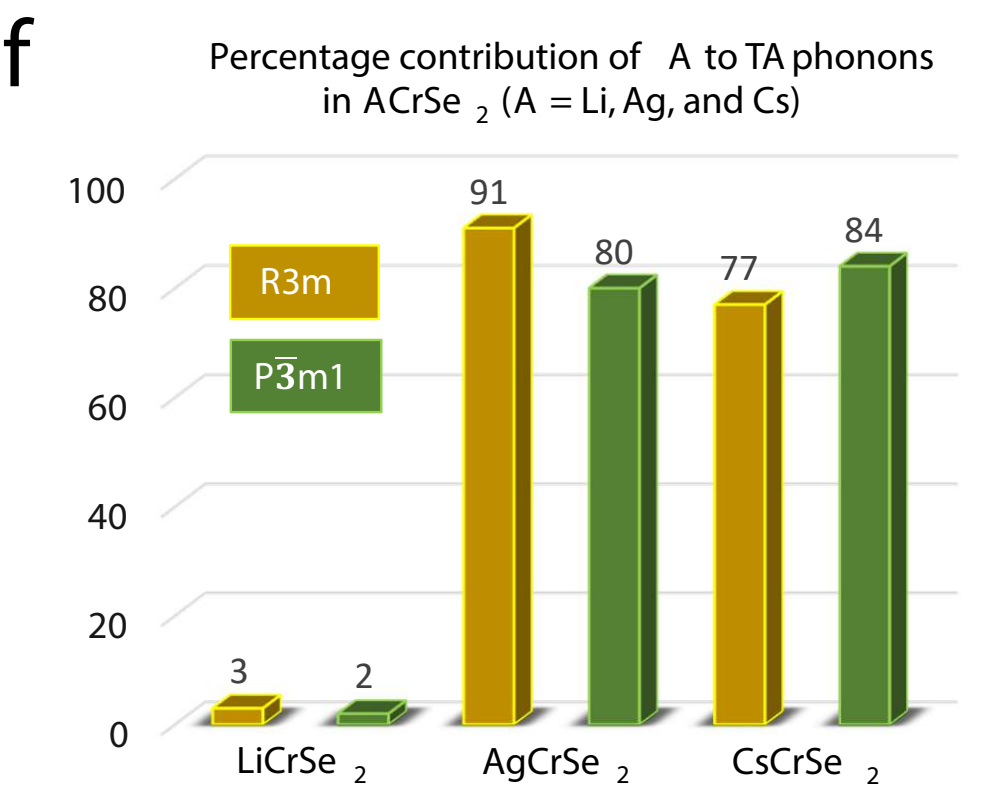
Percentage contribution of A to TA phonons
in ACrSe$_2$ (A = Li, Ag, and Cs)
R3m
P$\bar{3}$m1
3
2
91
80
77
84
LiCrSe$_2$
AgCrSe$_2$
CsCrSe$_2$

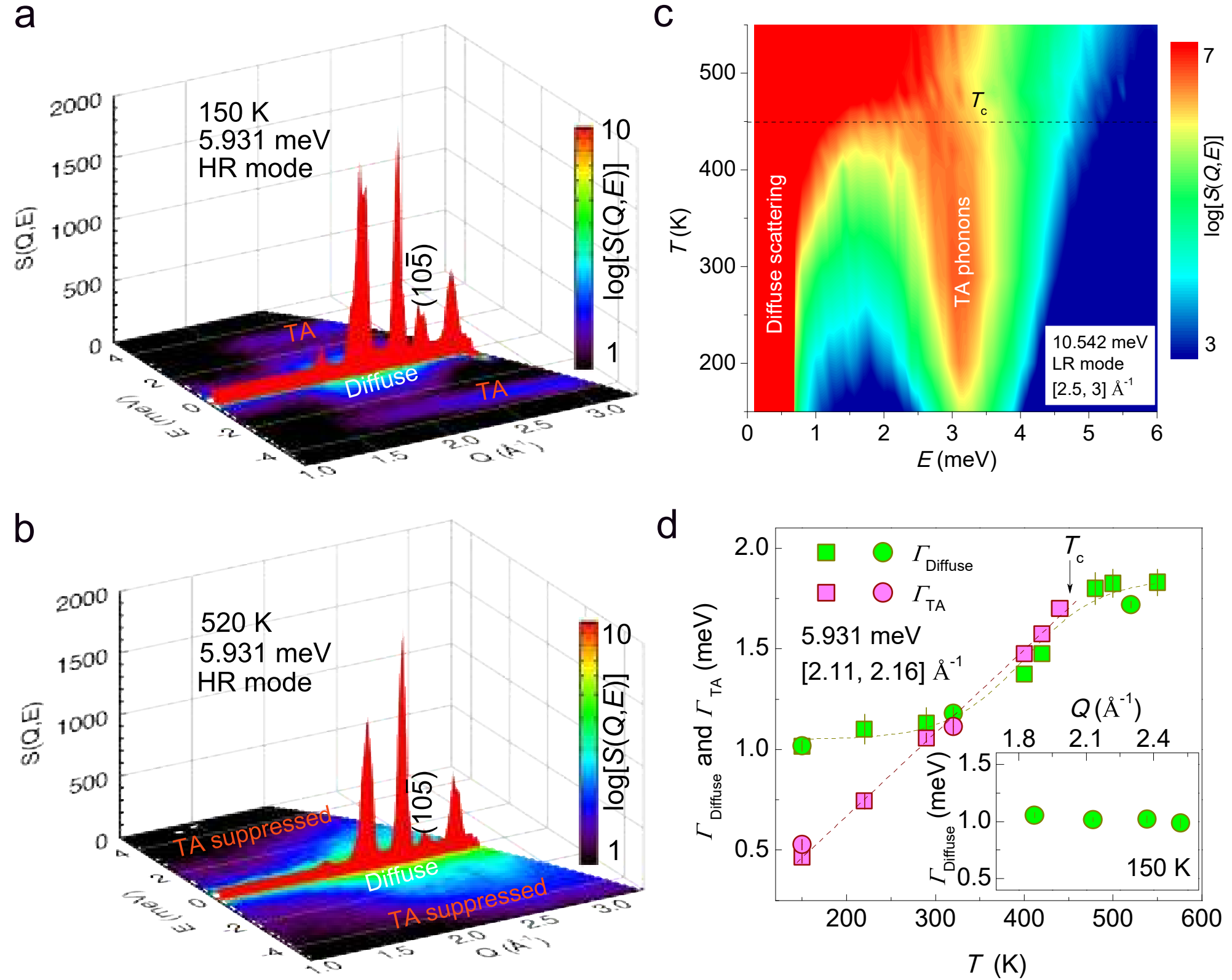
a
150 K
5.931 meV
HR mode
S(Q,E)
2000
1500
1000
500
0
TA
Diffuse
TA
(10$\bar{5}$)
10
1
log[S(Q,E)]
E (meV)
Q (Å$^{-1}$)
b
520 K
5.931 meV
HR mode
S(Q,E)
TA suppressed
Diffuse
TA suppressed
(10$\bar{5}$)
c
$T_c$
Diffuse scattering
TA phonons
10.542 meV
LR mode
[2.5, 3] Å$^{-1}$
T (K)
E (meV)
log[S(Q,E)]
d
$\Gamma_{Diffuse}$
$\Gamma_{TA}$
5.931 meV
[2.11, 2.16] Å$^{-1}$
$\Gamma_{Diffuse}$ and $\Gamma_{TA}$ (meV)
T (K)
Q (Å$^{-1}$)
150 K

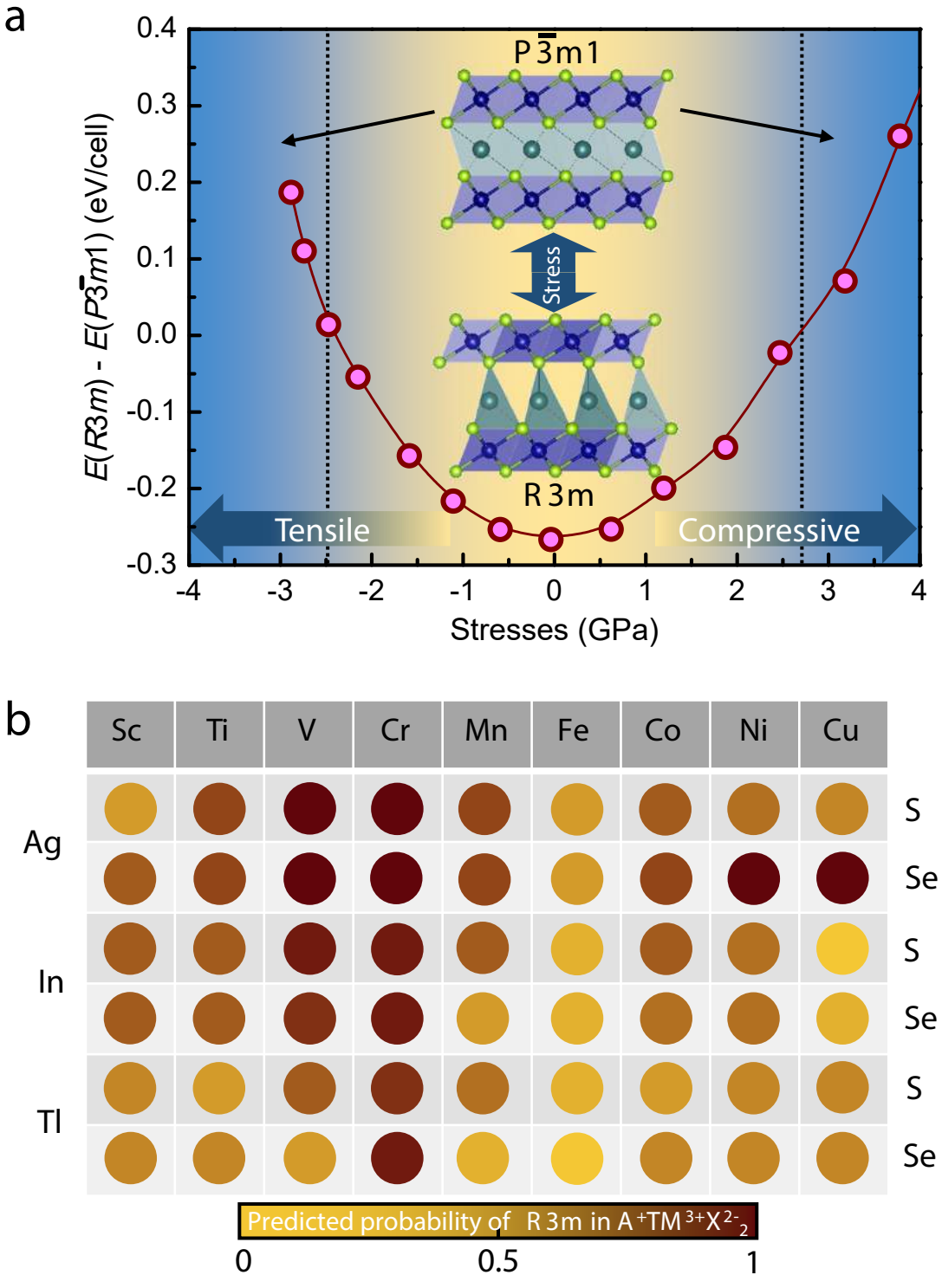
a
0.4
0.3
0.2
0.1
0.0
-0.1
-0.2
-0.3
E(R3m) - E(P3̄m1) (eV/cell)
P 3̄m1
Stress
R 3m
Tensile
Compressive
-4
-3
-2
-1
0
1
2
3
4
Stresses (GPa)
b
Sc
Ti
V
Cr
Mn
Fe
Co
Ni
Cu
Ag
In
Tl
S
Se
S
Se
S
Se
Predicted probability of R 3m in A+TM3+X2-2
0
0.5
1